Check for updates

UV-cured nanocomposite coating for surface charging mitigation and breakdown strength enhancement: exploring the combination of surface topographical structure and perfluorooctyl chain†

Chao Wang, [ID] Wen-Dong Li, Zhi-Hui Jiang, Xiong Yang, Guang-Yu Sun and Guan-Jun Zhang*

A facile method using a nanocomposite coating is proposed to suppress surface charge accumulation and enhance the surface breakdown strength of polymeric insulating materials like epoxy resin, by covering a thin 1,1,2,2-tetrahydroperfluorodecyltrimethoxysilane modified alumina (Al_2O_3) flake/UV curable resin nanocomposite coating. Due to the peculiar characteristics of perfluorooctyl chains at the microscale and the intricate topographical structure of morphology at the mesoscale, the coating exhibits enhanced water/oil repellence, surface charge accumulation resistance, and flashover withstanding capability. It is found that increasing the content of modified Al_2O_3 is conducive to decreasing the surface free energy of the specimens, rendering them superhydrophobic. Experimental tests in air show that the presence of nanoparticles generates numerous carrier traps at the surface layer, contributing to a much faster charge decay rate. Furthermore, impulse flashover voltage tests under vacuum show a >100% improvement of surface electrical strength. Further experimental results reveal that lower secondary electron emission yield remarkably alleviates the surface charging phenomenon, thus relieving electric field distortion caused by hetero-charges. We envision that such a multifunctional strategy for surface discharge mitigation is efficient, adaptable and easy to scale up, and thereby exhibits great prospects for applications in electronics and electrical power systems.

1. Introduction

Complex service environments subject polymeric insulating materials to a variety of hazards concurrently. Apart from mechanical and thermal stresses, surface discharge could lead to insulation failure, incurring catastrophic consequences to various devices like spacecraft,[1] pulsed power equipment,[2] power delivery equipment,[3,4] *etc.* Fig. 1 (left). This phenomenon poses a formidable challenge with respect to compact designs and higher operating voltage level demands in insulation systems. Many theories have revealed that the build-up surface charges under the actual operating environment incline to aggravate field distortion and cause surface discharge at lower voltages, which could further deteriorate the insulation

performance. Fig. 1 (middle) illustrates the possible charge behaviors (generation and dissipation) occurring at the dielectric surface. Apparently, the source of surface charge is multitudinous: *e.g.* triboelectrification,[5] field emission,[6] secondary electron emission (SEE),[6,7] near-surface gas ionization,[8] *etc.* Particularly, SEE and gas ionization usually are considered as the main reasons for charge accumulation in vacuum/insulator and gas/insulator system, respectively. Meanwhile, many factors like humidity,[9,10] surface conductivity,[10] and neutralization contribute to the dissipation of accumulated charge. Surface charges also dissipate when migrating towards the material bulk. In the past decades, numerous studies have been dedicated to efficient suppression of surface charging from two main aspects: *i.e.* inhibiting generation and accelerating dissipation, summarized in Fig. 1 (right). On the one hand, for an insulation system, decreasing the maximum electric strength and controlling field direction by geometry design,[11] dielectric graded material,[12] or nonlinear fillers[13] can reduce charge generation caused by field emission or gas ionization, and facilitate surface charge carriers decay under the modulated electric field, respectively. On the other hand, strategies aimed at material surface are comparatively more universal and

State Key Laboratory of Electrical Insulation and Power Equipment, School of Electrical Engineering, Xi'an Jiaotong University, Xi'an 710049, China. E-mail: gjzhang@xjtu.edu.cn
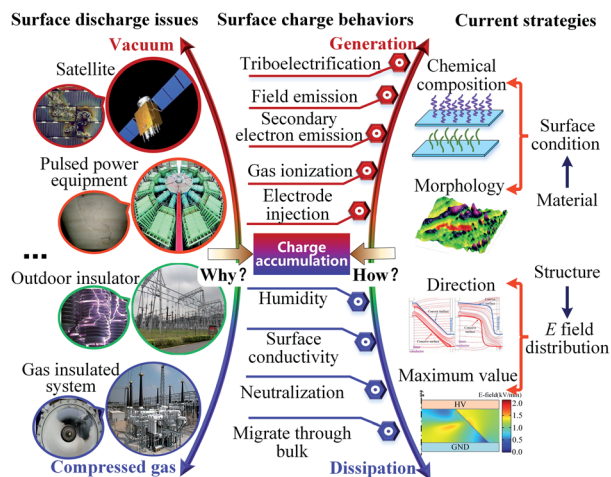
Fig. 1 A list of the practical applications, fundamental mechanisms for surface charge generation or dissipation, and general strategies for surface electric strength enhancement of vacuum/solid or gas/solid interface.

adaptable. Previous researches indicated that surface physical states and chemical component are key factors that affect the generation and migration of charge carriers, Fig. 1 (upper-right). Intricate micro or macro topography created by plasma etching,[14] mechanical grooving[15] or polishing,[16] and laser shaping,[17] are used to set barriers for discharge development and improve conductivity to alleviate charge accumulation. Chemical functionalization methods including direct or plasma assisted fluorination,[18,19] radical elimination,[10] and nano fillers addition,[20] can suppress charge generation and accelerate dissipation as well.

All these methods, however, aim at a single objective (*i.e.* inhibiting surface charging from mono source or accelerating charge dissipation by mono way), resulting in poor universality and applicability due to the complexity of charging processes. For instance, methods to inhibit charge generated by tribo-electrification has been systematically studied from the mechanism to application, and has been comprehensively reviewed in ref. 21 and 22. Nonetheless, some other processes in Fig. 1 are also accompanied by the consecutive formation of surface charges. Moreover, unfavorable conditions like dust deposition and icing may lead to insulation failure as well.[23] It is also notable that a recent advancement in material design geared toward integration of multiple functions into one material.[24,25] This constructive strategy is universal, robust, and adaptable for dealing with real application scenarios. Is there a multifunctional strategy for effective suppressing surface charge accumulation, and improving surface electrical strength of insulator? To this end, a nanocomposite coating with excellent hydrophobicity, high surface electrical strength, fast charge decay rate, and low secondary electron emission yield (SEEY) is prepared by UV curing process. Compared to thermal curing technique, photo-polymerization is efficient (fast curing speed) and energy-saving (operating at room temperature), and therefore has been widely used in various fields related to surface engineering.[26,27] Here,

fluorocarbon modified Al_2O_3 flakes were blended with UV curable resin, synthesizing a new type of composite which could be cured under UV light illumination. Comparing with other nanoparticles, nano-Al_2O_3 in the form flakes has larger specific surface area, which benefits the fabrication of this multifunctional coating. Finally, the interplays among surface topographical structure at mesoscale and perfluorooctyl chain at microscale, surface charge behavior and surface breakdown strength in vacuum and atmospheric environment were further analyzed. It is believed that this efficient, adaptable and multifunctional approach overcomes the challenges of conventional surface treatment techniques and shows huge potential to be widely used in a variety of energy and electronic applications.

2. Experimental section

2.1. Preparation of nanocomposite coating

Initially, nano Al_2O_3 was prepared by a liquid method (detailed preparation technique and characterization results are shown in the ESI Section A†). On the one hand, the prepared flakes with large specific surface area contribute to the surface modi-fication and morphology alternation. On the other hand, flakes can form abundant inorganic/organic interfaces to enhance charge dissipation and to protect insulator surfaces from hot electron bombardment.[28] In our previous researches, we found that fluorinated chains with alkyls structure can decrease surface free energy and enhance surface electrical strength.[29,30] Hence, silane coupling agent (1,1,2,2-tetrahydroper-fluorodecyltrimethoxysilane, FAS17) was grafted at the nano-particles surface to serve as fluorination layer. Also, to guarantee strong bonding strength between fillers and matrix, inorganic fillers are usually modified by chemical groups that can react with the matrix. With these considerations, silane coupling agents including FAS17 and γ-methacryloxypropyl trimethoxy silane (KH570) were grafted at the surface of Al_2O_3 particles. Then the modified nanoparticles were loaded to the UV curable resin to prepare nanocomposite. Finally, these photo-curable nanocomposites were sprayed to the surface of epoxy resin (a commonly used material in electronic/electrical systems), and then cured in a customized UV-curing chamber to obtain a thin film on the insulator's surface. More details about the preparation process are shown in ESI Section B.†

2.2. Characterization of surface morphology, chemical composition, and wettability

Morphologies of nanoparticles before and after surface modi-fication were observed by transmission electron microscope (TEM, JEOL JEM2100F). Crystalline structure of the inorganic fillers was characterized by XRD (Bruker D8-Advance, Karls-ruhe) with Cu-Kα radiation. Scanning range of diffraction angle (2θ) was from $10°$ to $70°$ stepped by $0.02°$ per second. Fourier transform infrared spectra (FTIR, Thermo Fisher Nicolet iN10) was recorded to characterize surface groups of the nano-particles. XPS (Thermo Fisher ESCALAB Xi+) were measured to confirm the segregation of fluorinated chains. The surface morphology of the coating was characterized by field emission

scanning electron microscope (SEM, ZEISS GeminiSEM 500). In addition, the cross-sectional morphology after liquid nitrogen freezing was characterized by SEM (VE-9800S). Laser scanning confocal microscope (LSCM, Olympus LEXT OLS4000) was applied to characterize 3D morphology of the coating. Further, the measurement of average roughness (R_a) was performed on a contact type instrument (MarSurf M 300C, Germany). To test for water/oil repellence, ~1 μL deionized water and diiodo-methane droplets were dispensed toward the coating surface. Then the static contact angle was recorded by optical contact angle measuring device (KRUSS DSA100S).

2.3. Surface conductivity, charge decay, secondary electron emission, charge distribution and electrical strength characterization

Surface conductivity measurements were conducted by a pico-ampere meter (6517B, Keithley) with 8009 standard fixture. The measurements of SEEY were performed in a high vacuum chamber (<5 × 10^{-4} Pa) including an electron gun (EGL-2022, Kimball), producing electron beam with energy from 50 eV to 5 keV. Electrical strengths in air and vacuum were characterized by a self-designed system, which can generate impulse voltage up to 80 kV. Surface potential distribution after the impulses was measured by an electrostatic voltmeter (Trek341B) connected by a vibrating Kelvin probe (Trek 3455ET), with the probe scanning in a region of 48 × 30 mm. In the same way, surface charge decay at a single point was also recorded by the electrostatic voltmeter. All the experimental details about these electrical properties characterizations can be found in the ESI Section C.†

3. Results and discussion

3.1. Characterization of prepared nanoparticles

Characterization results of morphologies (Fig. S1a, ESI†) from TEM show that the prepared particles have flaky structure with average size of 27.6 nm and the average thickness is about 4.3 nm (detailed statistical approach are described in the ESI Section A†). X-ray diffraction (XRD) analysis (Fig. S1c†) shows that the nano-particles have multiple peaks at $2\theta = 20, 32.7, 37.2, 39.5, 45.8, 61,$ and 67°, which are the typical reflections of γ-Al$_2$O$_3$. The crucial factor of this multifunctional coating lies in the preparation of perfluorooctyl chain grafted nano Al$_2$O$_3$ flakes (Fig. 2a). The covalent linkage of silane coupling agents including FAS17 and KH570 to Al$_2$O$_3$ flakes were confirmed by TEM observations and Fourier-transform infrared (FT-IR) spectra. The inset of Fig. S1b† shows an amorphous layer with a thickness of about 3 nm outside the Al$_2$O$_3$ nanoparticles. Intuitively, silane coupling agents have been successfully coated onto the surface of the nanoparticles. The FT-IR result of KH570 + FAS17@Al$_2$O$_3$ in Fig. S1d† shows many peaks comparing with that of pristine Al$_2$O$_3$. Apart from the obvious peak around 3400 cm^{-1} (–OH), additional peaks appearing at 2945, 2850, 1723, 1640, 1247, 1205, and 1095 cm^{-1} should attribute to –CH$_3$, –CH$_2$, –C=O, –C=C, –CF$_3$, –CF$_2$, and –C–O–C, respectively.

3.2. Characterization of UV-cured resin/modified Al$_2$O$_3$ composite

3.2.1. Surface morphology. Upon UV radiation, a thin film is generated at the surface of the dielectric substrate. Side-view scanning electron microscopy (SEM) images in Fig. 2b and c
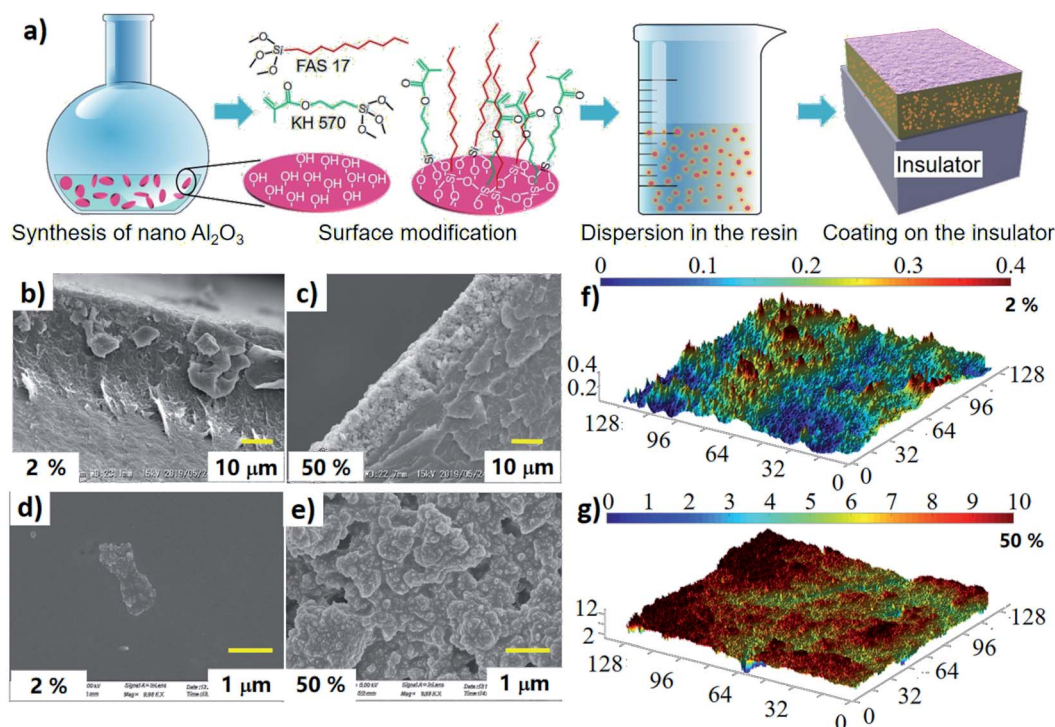

Fig. 2 Experimental designs and featured morphologies of the UV curable composite coating. (a) Synthetic scheme of UV-cured composite coating. (b) and (c) Cross-sectional SEM, (d) and (e) superficial SEM, (f) and (g) 3D morphology images of UV-F-2% and UV-F-50%, respectively.

show that the coating layer has a uniform thickness of ≈20–30 µm. Observations of surface morphology indicate that these nanoparticles with flake size in the resin serve as modifiers at the surface of the coating, which remarkably increases the roughness with the improvement of loading rate. Note that specimens prepared with different loading ratios (i = 2%, 5%, 10%, 30%, 50%) are denoted as UV-F-i. Compared with specimen with low loading ratio (2%, Fig. 2d and S2b†), doping more Al_2O_3 flakes (50%, Fig. 2e and S2c†) form numerous pores, valleys, and pits at mesoscale. Characterization of 3D morphology based on LSCM shows that coating with 50% loading ratio (Fig. 2g) exhibits considerable roughness comparing with that of UV-F-2% (Fig. 2f). Furthermore, the monotonous increase of average roughness (R_a in Table S3†) with Al_2O_3 amount is consistent with the observations of surface morphologies.

3.2.2. **Surface chemical composition and hydrophobicity.** As mentioned above, apart from surface geometric topology at mesoscale, another key factor for this multifunctional strategy lies in the modification of the nanoparticles. X-ray photoelectron spectra (XPS) results show that low surface energy fluorinated chains (FAS17) grafted at the surface of nanoparticles are presented at the coating surface after photopolymerization. In the case of low loading ratio (UV-F-2%), no peak is observed at F 1s position in Fig. 3a as few flakes are segregated to the surface. In contrast, UV-F-50% exhibits a strong F 1s peak in widen scan spectra. Analyses on C 1s core-level spectra further confirm the presence of fluorinated chains. Besides the peaks in 284.8 (C–C), 286.4 (C–O–C), and 288.6 eV (C=O) in Fig. 3b, additional peaks in Fig. 3c at 291.7 and 293.8 eV are attributed to the –CF_2 and –CF_3 groups, respectively. O 1s spectrum of UV-F-2% (Fig. S3a†) shows two peaks at 532 eV (C–O) and 533.7 eV (C=O), while no peak is observed in F 1s spectrum (Fig. S3b†). In

contrast, O 1s spectrum of UV-F-50% (Fig. S3c†) shows two new peaks at 531.1, and 532.97 eV, which should be contributed to Al_2O_3 fillers and Si–O groups in silane coupling agents, respectively. By the same token, strong peaks appear in F 1s spectrum because of the presence of C–F chains (Fig. S3d†). FT-IR spectra of the coating were measured at attenuated total reflection (ATR) mode (Fig. S3e†). The decrease of peaks strength in 1728.8 cm^{-1} (–C=O), 1467.5 and 1452.1 cm^{-1} (–CH_2 and –CH_3), 1200.5 cm^{-1} (O=C–O–C) and 1112.7 cm^{-1} (–C–O–C), and the presence of –CF_2 peak at 1095 cm^{-1} indicate that the amount of modified nanoparticles in the UV-cured composite layer is increased. Photographs of water and diiodo-methane droplets on the coating surface are presented in Fig. 3d and e, respectively. Interestingly, liquid contact angle is not in a linear relationship with the fillers loading ratio in the preparation of the coating layer. This should be ascribed to the difference of roughness shown in Table S3.† At very low loading ratio (2%), surface wettability is mainly determined by surface chemical composition since the amount of nanoparticles is small. In this case, hydrophobic surface benefits from the chemical groups with low surface energy. With the increase of loading ratios, the distance among nanoparticles further decreases, droplets tend to contact directly with the surface when the air escapes out of the roughness, transiting into a Wenzel wetting state (smaller contact angle is observed in this stage). When fillers loading ratio further increases (≥30%), nanoscale roughness is generated. A thin layer of air is trapped between the solid surface and the liquid, transiting into a Cassie state.[31,32] In this case, an increase in the amount of nano fillers employed in the initial mixture produces surfaces with higher contact angle. As shown in Fig. 3f, UV-F-50% has very low surface energy of 1.90 mN m^{-1} as compared with the 14.45 mN m^{-1} of UV-F-2, and the maximum water contact angle achieve up to 153.64°. This
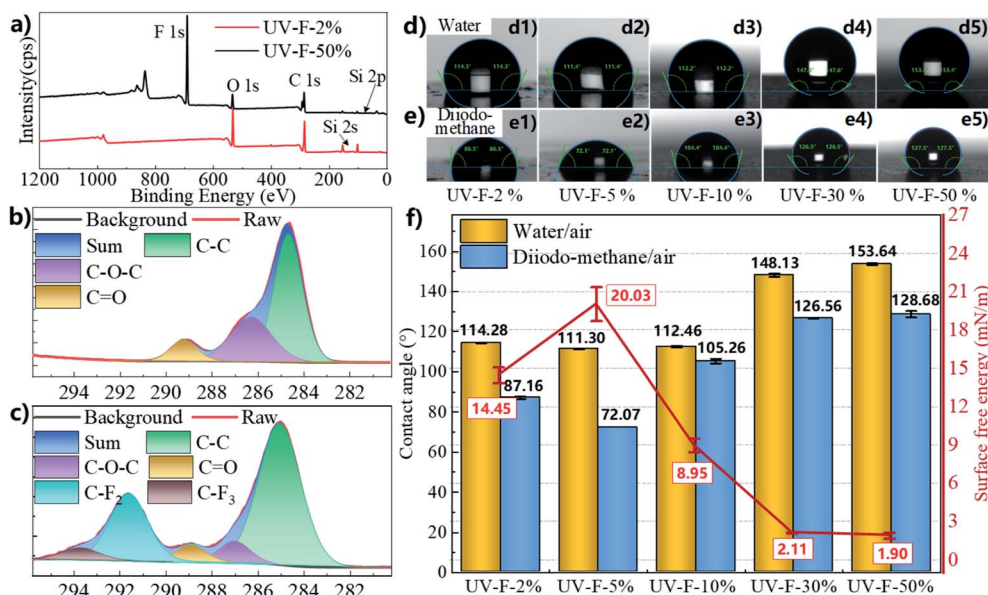

Fig. 3 (a) XPS scans of UV-F-2% and UV-F-50%. C 1s envelopes of (b) UV-F-2% and (c) UV-F-50% with prominent C–F_2 and C–F_3 peaks, indicating the presence of FAS 17 at the surface. (d) and (e), respectively, photographs of water and diiodo-methane droplets on the coating surface at different loading ratios. (f) Values of contact angle and surface free energy of the coating.

superhydrophobic function has the potential to protect dielectric from moisture absorption and icing or frosting in some special circumstances.[33]

3.3. Electrical performance

3.3.1. Flashover and charge dissipation in air. Air/solid dielectric parallel insulation system are commonly used in the electrical power system and power electronic circuitry. Partial discharge caused by strong E field at local region generates surface charges, thus deteriorating the insulation performance in the long term. Fig. 4 shows the surface electrical strengths and surface charge behaviors of the nanocomposite coating in air. Characterization strategies and experimental setups are described in ESI Section B.† As we mentioned in the ESI,† three indexes (first flashover voltage (U_{fb}), conditioned voltage (U_{co}), and hold-off voltage (U_{ho})) were used to evaluate the surface flashover characteristics of the testing specimens at different stages. Invariably, negative lightning impulse voltage (waveform depicted in Fig. S6c†) is adopted to characterize the flashover strength of the specimens in this paper. Dashed lines with different colors in Fig. 4a represent the corresponding flashover voltages of pristine epoxy without coating. In general, this nanocomposite coating can effectively enhance the surface

breakdown strength in air. With a stepwise increase of the fillers content in the composite, the flashover voltages improve gradually and become stable at a relatively high level. UV-F-50% displays the highest U_{fb} of 13.2 kV (absolute value), increased 10% compared to the UV-F-2%. U_{co} shows the highest flashover voltage comparing with the other two parameters, and the maximum value of U_{co} reaches to 14.3 kV. In this stage, the surface breakdown mainly happens in air because the average E field is close to 3 kV mm^{-1} (critical E field of air breakdown). The 17% improvement of U_{ho} is supposed to be caused by the arc resistance discrepancy of specimens during discharge process. Because of the excellent thermal conductivity, radiation resistance, and high chemical stability of inorganic flakes, Al$_2$O$_3$ fillers in the nanocomposite coating protect the insulator surface from direct bombardment of hot electrons and photon radiations during the discharge process. Hence, after multiple flashover times, the surface electrical strength of specimens with high loading ratios can be maintained. Additionally, surface electrical conductivity measured is modulated over several orders of magnitude for the same reason (Table S3†). As a consequence, different surface charge decay rates were observed. After applying a negative voltage to the specimen with 100 times (−16 kV), strong E field at the cathode triple junction
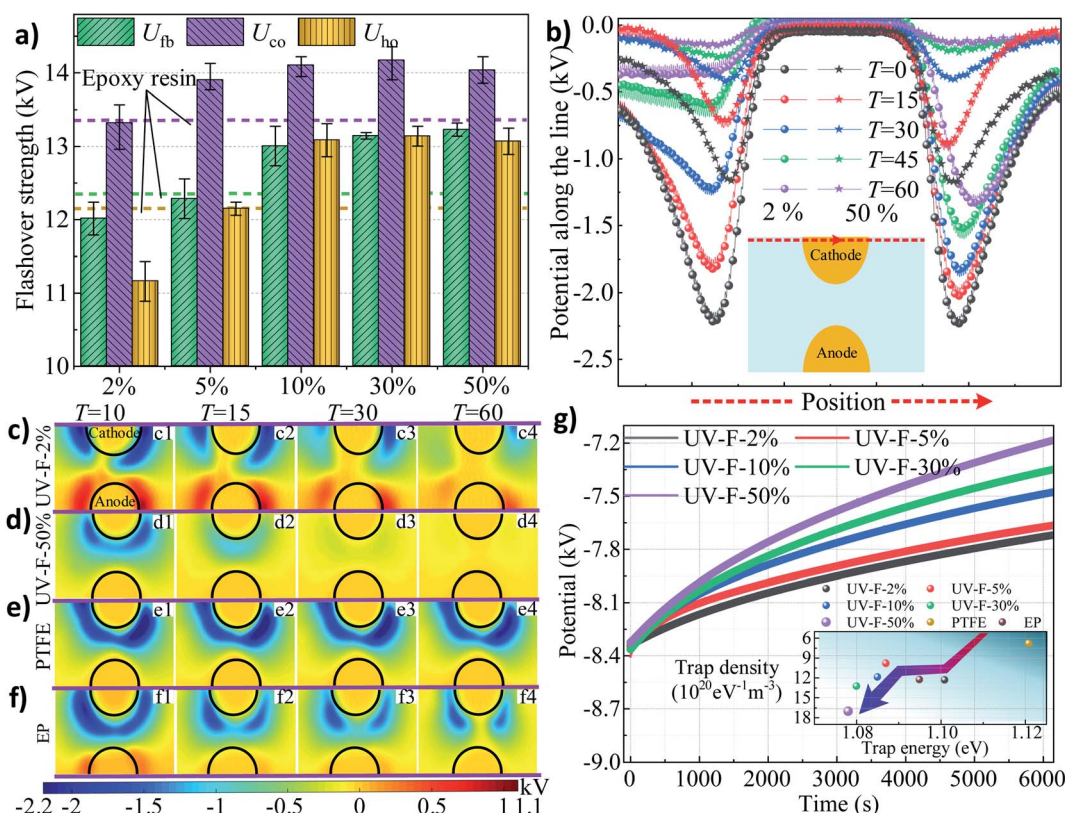

Fig. 4 Experimental results in atmosphere. (a) Impulse flashover voltages of specimens with different fillers content. (b) Variations of surface potential of UV-F-2% and UV-F-50% along a line with time. The inset is the illustration of electrode/insulator layout, and the position of the line. Overall potential distribution of (c) UV-F-2%, (d) UV-F-50%, (e) PTFE, and (f) EP within different decay time. The length of decay time after the pulses is denoted as T. (g) Surface potential decay profiles for UV-F series during surface traps measurement process. The inset displays the comparisons of trap peak position among UV-F-x%, PTFE, and EP. Higher trap density and lower trap energy level means faster surface charge dissipation.

(where the electrode, insulator, and gas meets) causes gas ionization, and homo-charges are deposited at the insulator surface, establishing negative potential in the ambient environment. Variations of specific potential of UV-F-2% and UV-F-50% values along a line (the red dashed one near the cathode shown in the inset of Fig. 4b) with time are shown in Fig. 4b. As time progresses, UV-F-50% shows faster surface charges decay rate comparing with that of UV-F-2%. The maximum potential (absolute value) of UV-F-50% along the line decays to zero within one hour. In contrast, the residual charges on UV-F-2% still maintain at a high level (−1.5 kV after 60 minutes). Overall potential distributions are shown in Fig. 4c and d. Meanwhile, common polymeric insulating materials like polytetrafluoroethylene (PTFE), and epoxy (EP) are used as reference objects for illustrating the effectiveness of this multifunctional coating. The surface charge behaviors of these specimens are shown in Fig. 4c–f. In general, PTFE shows the minimum initial potential (−2.47 kV) and the lowest decay rate (about 0.3 kV h^{-1}) at the same temporal scale. This should be attributed to the fact that charges, once deposited on fluoropolymer, remain stable in the materials. In contrast, EP and UV-F-2% show the similar initial potential distribution and potential decay rate. Particularly, for the UV-F-50%, the initial potential is very low (−1.2 kV) and there are much fewer charges left on the surface after 1 h. This phenomenon is in good agreement with previous conclusion that nanocomposites with high loading ratio can facilitate the charge dynamics faster charge carriers transport.[34]

Isothermal surface potential decay (ISPD) of UV-F series measured by electrometer are shown in Fig. 4g. Not surprisingly, with the increase of fillers content, surface charge decay rate also increases rapidly. According to the surface electron trap information calculated by ISPD method,[35] shallower traps are introduced to the surface by coating this nanocomposite layer (the inset of Fig. 4g). The trap energy peak shifts from original 1.11 eV (UV-F-2%) to 1.07 eV (UV-F-50%) and the trap density increases from 12.35×10^{20} to 17.32×10^{20} eV^{-1} m^{-3}. Note also that the PTFE shows deepest trap level and the minimum traps density. It should be the intrinsic physical mechanisms that account for the differences of surface charge decay rate. The fast charge decay property of the coating is supposed to be another useful function for the insulator, which can keep desirable voltage in targets and protect them from charge accumulation especially in dc voltage conditions.

3.3.2. Flashover and charge accumulation in vacuum. To further embody the versatility of this multifunctional coating, electrical properties in vacuum are systematically investigated. As a matter of routine, three indexes are used to estimate the surface electrical strength of the specimens, and dashed lines in Fig. 5a indicate the flashover voltages of pristine epoxy. The flashover voltages (absolute value) of the specimens are improved from 12.7 to 37.8 kV, varying with their fillers loading ratios. In detail, U_{fb}, U_{co}, and U_{ho}, respectively, can be increased by 75% (19.4 to 33.9 kV), 94% (19.3 to 37.1 kV) and >150% (12.7 to 34.3 kV) in the maximum when the fillers loading ratio rising up to 50%. This significant improvement of surface flashover strength suggests an underlying interplay between surface states and discharge development process. After applying −30

kV impulse voltage to the specimen, SEE avalanche renders insulator surface positively charged. Specific potential variations of UV-F-2% and UV-F-50% values along a line (the red dashed one near the cathode shown in the inset of Fig. 5b) with impulse times are shown in Fig. 5b. Apparently, the initial potential of UV-F-2% (approximated 5 kV) is much higher than that of UV-F-50% (below 200 V) in the case of N equals 1 (variable N represents the number of impulse times). During the next impulse process, stronger field emission generates more initial electrons, due to the field enhancement caused by accumulated hetero-charges, resulting in intense SEE avalanche. Hence, charges on the surface gradually accumulate as N increases, which then saturated when N is equal to 50. The highest surface potential of UV-F-2% is up to 6.8 kV for the scenario that N equals 200. Conversely, higher filler loading ratio (UV-F-50%) exhibits excellent charge suppression capability that the highest surface potential is limited to 2.5 kV under the same testing conditions. The overall potential distributions are shown in Fig. 5c and d. As above, for comparison, experimental results of PTFE and EP are demonstrated in Fig. 5e and f, respectively. Evidently, for UV-F-2%, PTFE, and EP, the surface charge behaviors are analogous. After multiple pulse voltage strikes ($N = 1$, 5, 10, and 50), the amount of surface charges progressively increases, and similar surface potential distribution is generated by those charges when N is equal to 50 (the maximum potentials for UV-F-2%, PTFE, and EP are, 7.0, 6.7, and 6.5 kV, respectively). In the case of UV-F-50%, little change is observed from the surface potential distribution until $N \geq 50$, indicating that few electron impacts occur in SEE-induced avalanche (i.e. multipactor) process. With the increases of pulse times and applied voltage, more electrons escape from the surface, thereby slightly increasing surface potential (Fig. S9, ESI†). But invariably, the maximum values of surface potential are all below 4 kV, indicating that the amount of surface charge still maintains at a very low level. These differences in surface charge accumulation characteristics are well-agreeable with the measurement results of SEEY (Fig. 5g) on the experimental platform shown in Fig. S4.† More precisely, UV-F-50% possesses a much lower SEEY profile comparing with UV-F-2%, resulting in less electrons emission to the vacuum. Hence, the originally neutral dielectric surface barely accumulates positive charges. δ_{max} is the peak point in the SEEY curve. Fig. 5h displays the positions of δ_{max} for UV-F-2%, UV-F-5%, PTFE, and EP. A positive correlation is found between the distance of δ_{max} to the origin and maximum potential in Fig. 5c4–f4. UV-F-50% is close to the origin of coordinates with δ_{max} of 1.67, and the maximum potential in Fig. 5d is lower than that of other specimens, corresponds to the >100% improvement of flashover voltage. On the contrary, because of the largest primary electron energy (A_{max}) of 500 eV, UV-F-2% presents the highest surface potential in Fig. 5c. Between these two extremes, although EP exhibits a highest δ of 2.36 versus 2.04 of UV-F-2%, its corresponding A_{max} is 300 eV, which accounts for the lower surface potential. We believe that this significant suppression of surface charging in vacuum is an extremely important property for electrical/electronic equipment where SEE dominates the discharge process.[36]
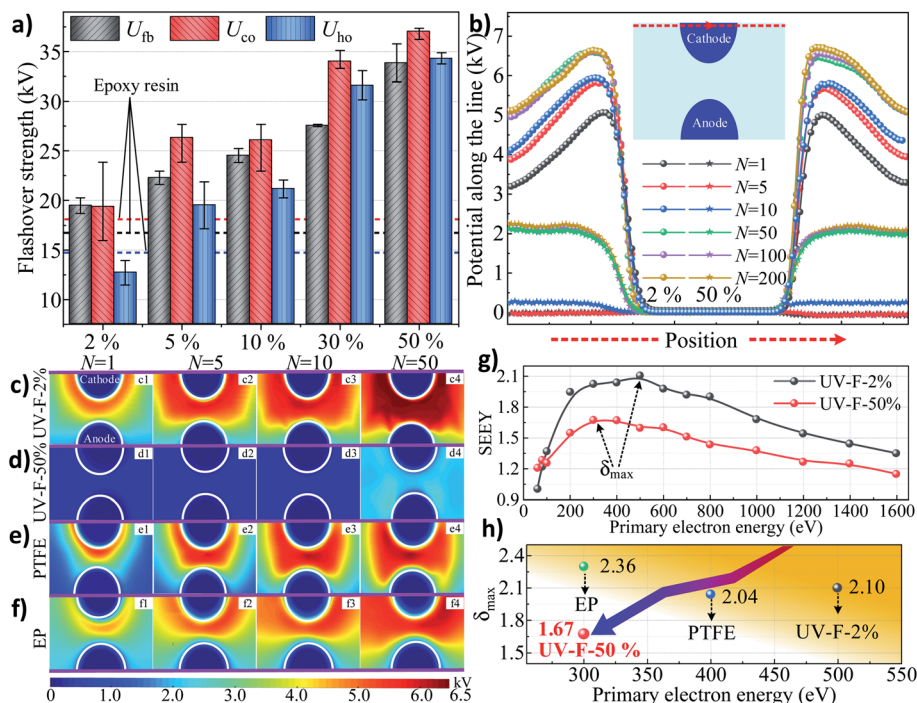
Fig. 5 Experimental results in vacuum. (a) Impulse flashover voltages of specimens with different fillers content. Potential distribution of (b) variations of surface potential of UV-F-2% and UV-F-50% along a line with pulse time. The inset is the illustration of electrode/insulator layout, and the position of the line. Overall potential distribution of (c) UV-F-2%, (d) UV-F-50%, (e) PTFE, and (f) EP after applying −30 kV voltage with different times. The number of pulses times is denoted as N. (g) SEEY profiles of UV-F-2% and UV-F-50%. (h) The comparisons of δ_{max} position among UV-F-2%, UV-F-50%, PTFE, and EP. Lower δ_{max} and the corresponding primary electron energy means less surface charge accumulation.

3.4. Physical model establishment and mechanism explanation

A multiscale integrated physical model is established to elaborate the interplay between the surface states of the coating layer and discharge development or the following charge migration process. A typical insulation system is shown in Fig. 6a. High voltage (HV) source generates the E field between anode and cathode at the specimen surface. At the mesoscale ($\mu m \sim mm$), surface morphology could be altered by adding inorganic fillers, and the roughness level can be modulated from nm to μm (Fig. 6b). Regarding microscale ($\text{Å} \sim nm$), the C–F chains grafted at the nanoparticles' surface form a fluorinated layer with a thickness of 3 nm (Fig. 6c). These surface characteristics at different scale have strong correlation with the surface charge behaviors.

In gas atmosphere, gas ionization accounts for the sources of surface charge. It needs to be mentioned that negative charges are accumulated at the surface because more electrons than ions enter the solid boundary during plasma sheath formation (Fig. 4), thus only electron dynamics is discussed here, and the positive charge transport is not considered in the present work. Previous researches indicate that hopping transport mechanism is well-accepted for explaining electrical behavior in insulating polymers and understanding charge transport in disordered semiconductors and amorphous solids.[37] These theories assume that the motion of electrons through the insulator is governed by availability of localized states.

Topological and chemical disorder can break the symmetry of the ordered system, forming localized states which concentrate in band tails.[38] In the case of UV-F-2% (Fig. 6d), once charges are deposited on the surface, few energy traps can be provided for charge transportation since the amount of Al_2O_3 flake is limited. For UV-F-50%, physical defects like corners, pits, and pores can serve as shallow traps. Additionally, chemical disorder caused by C–F chains can be considered as relatively deeper traps. These localized states provide numerous paths for
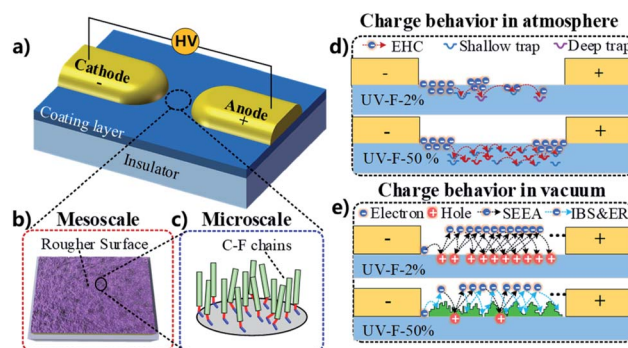

Fig. 6 Physical model for the nanocomposite coating. (a) Insulation system with a cathode and anode bridging along the insulator surface. (b) Surface topological structure at mesoscale. (c) Surface molecular structure at microscale. (d) Physical model for describing charge behavior in atmosphere. (e) Physical model for describing charge behavior in vacuum.

electron jumping, resulting in faster charge decay rate comparing with that of UV-F-2%.

In vacuum, surface charging mechanism is totally different. As shown in Fig. 6e, the surface of UV-F-2% is very smooth, electrons emitted from the cathode are sufficiently accelerated by the applied E field before reaching insulator. Hence, incident electrons can easily penetrate into the interior of the composites due to the relatively high energy, and only few of them are reflected at the surface by inelastic backscattering and elastic reflection (IBS & ER). Thereafter, SEE avalanche contributes to electron loss for the material, leaving abundant holes on the surface. These positive charges provide recombination center for the subsequent incident electrons. Finally, a self-sustained SEE situation is reached where SEEY is equal to 1. In contrast, rougher surface of UV-F-50% decreases the electron collision mean free path before impacting the insulator surface. Free electrons gain limited energy from the E field, hence, hindering the development of SEE avalanche to some extent. Also, barriers set by the intricate morphology can induce multiple IBS & ER process at each interface for the newly created secondary electrons, which also contribute to the absorption attenuation of incident electrons. At microscale, factors like surface molecular chain also play a role for charge transport. C–F chains can act as electron traps to absorb electrons due to the strong electron affinity of fluorine atoms, thereby reducing the number of secondary electrons. To sum up, it is because of the synergistic effect of surface morphology and fluorinated chains that leading to different SEE efficiencies and surface potential under the same level of excited voltage.

3.5. Comparison of flashover mitigation strategies reported in recent literature with our work

To fully exhibit the great advantages of this research in the industrial applications, a comparison is carried out between the flashover mitigation strategies reported in recent literatures and experimental works in this paper. Flashover voltage (U_{ho}) improvement ratio in vacuum, and other factors of direct fluorination,[39] Mechanical polishing,[40] plasma etching,[14] laser grooving[41] are compared and the corresponding results are summarized in Fig. 7. Note that the other factors consideration

means a comprehensive evaluation including cost, process adaptability and functional diversity.

4. Conclusions

To summarize, a multifunctional strategy for the surface flashover mitigation of polymer insulating material is presented by the combination of surface topographical structure and perfluorooctyl chain. Low surface energy, low SEE, fast charge decay rate coating was fabricated through UV curing technique. UV curable resin with internal phase fractions as high as 50 wt% of fluorosilane modified alumina nanoparticles forms a thin film on the surface of insulator upon light radiation. The main findings could be listed as follows:

(1) Because of the micro/nano hierarchical structure generated by the nano Al_2O_3 flakes and the fluorinated chains grafted at Al_2O_3 surface, the coating exhibits the highest superhydrophobicity with a contact angle of 153° and surface energy of 1.90 mN m^{-1}.

(2) Furthermore, surface topographical features including corners, pits, and pores at the nano-/micro-scale leads to the considerable increase of shallow traps. ISPD results showed that the trap energy peak could shift from original 1.11 eV (UV-F-2%) to 1.07 eV (UV-F-50%) and the trap density increases from 12.35×10^{20} to 17.32×10^{20} eV^{-1} m^{-3}, thereby accelerating the dissipation of surface charge in air.

(3) Additionally, the noticeable roughening of surface features and drastic enrichment of fluorinated groups synergistically suppress secondary electron emission from 2.10 to 1.67. As a result, surface charging phenomena under impulse voltage strike are suppressed and flashover voltage U_{ho} increases from to 12.7 to 34.3 kV.

The present fabrication process features this technique efficient, and scalable, thus applicable for the high throughput preparation of more robust and reliable insulation systems without compromising the bulk characteristics.

Conflicts of interest

There are no conflicts to declare.

Acknowledgements

References

1 K. Toyoda, T. Okumura, S. Hosoda and M. Cho, *J. Spacecr. Rockets*, 2005, **42**, 947–953.
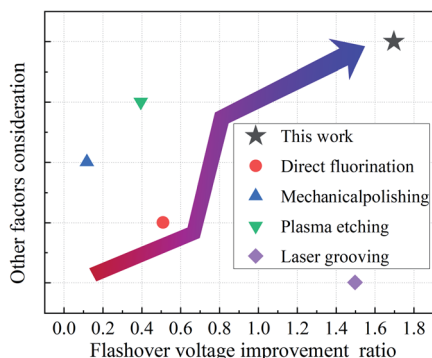2 G. J. Zhang, G. B. Su, B. P. Song and H. B. Mu, *IEEE Trans. Dielectr. Electr. Insul.*, 2018, **25**, 2321–2339.

Fig. 7 Comparison of different methods reported in recent literature with our work.

3 A. R. Verma and B. S. Reddy, *Eng. Failure Anal.*, 2019, **95**, 214–225.

4 B. Qi, C. Gao, C. Li and J. Xiong, *Int. J. Elec. Power.*, 2019, **105**, 514–520.

5 J. Wu, X. L. Wang, H. Q. Li, F. Wang, W. X. Yang and Y. Q. Hu, *Nano Energy*, 2018, **48**, 607–616.

6 G. Y. Sun, B. H. Guo, B. P. Song, G. Q. Su, H. B. Mu and G. J. Zhang, *Phys. Plasmas*, 2018, **25**, 9.

7 J. Z. Gleizer, Y. Krasik, U. Dai and J. Leopold, *IEEE Trans. Dielectr. Electr. Insul.*, 2014, **21**, 2394–2404.

8 A. A. Neuber, M. Butcher, H. Krompholz, L. L. Hatfield and M. Kristiansen, *IEEE Trans. Plasma Sci.*, 2000, **28**, 1593–1598.

9 K. W. Biegaj, M. G. Rowland, T. M. Lukas and J. Y. Y. Heng, *ACS Omega*, 2017, **21**, 576–1582.

10 H. T. Baytekin, B. Baytekin, T. M. Hermans, B. Kowalczyk and B. A. Grzybowski, *Science*, 2013, **341**, 1368–1371.

11 J. L. Wang, B. Yue, X. G. Deng, T. Q. Liu and Z. R. Peng, *IEEE Trans. Dielectr. Electr. Insul.*, 2018, **25**, 321–329.

12 W. D. Li, X. R. Li, B. H. Guo, C. Wang, Z. Liu and G. J. Zhang, *IEEE Trans. Dielectr. Electr. Insul.*, 2019, **26**, 1–9.

13 C. Li, C. Lin, J. Hu, W. Liu, Q. Li, B. Zhang, S. He, Y. Yang, F. Liu and J. He, *IEEE Trans. Dielectr. Electr. Insul.*, 2018, **25**, 1238–1247.

14 S. L. Chen, S. Wang, Y. B. Wang, B. H. Guo, G. Q. Li, Z. S. Chang and G. J. Zhang, *Appl. Surf. Sci.*, 2017, **414**, 107–113.

15 C. Chang, H. J. Huang, G. Z. Liu, C. H. Chen, Q. Hou, J. Y. Fang, X. X. Zhu and Y. P. Zhang, *J. Appl. Phys.*, 2009, **105**, 7.

16 J. Y. Xue, H. Wang, J. H. Chen, K. F. Li, Y. Q. Liu, B. P. Song, J. B. Deng and G. J. Zhang, *J. Appl. Phys.*, 2018, **124**, 11.

17 Z. P. Yan, X. D. Liang, I. Cotton and C. Emersic, *IEEE Trans. Dielectr. Electr. Insul.*, 2018, **25**, 1095–1102.

18 T. Shao, W. J. Yang, C. Zhang, Z. Niu, P. Yan and E. Schamiloglu, *Appl. Phys. Lett.*, 2014, **105**, 5.

19 F. Kong, C. Chang, Y. Y. Ma, C. Zhang, C. Y. Ren and T. Shao, *Appl. Surf. Sci.*, 2018, **459**, 300–308.

20 S. He, C. Lin, J. Hu, C. Li and J. He, *J. Phys. D: Appl. Phys.*, 2018, **51**, 215306.

21 L. F. Chen, Q. F. Shi, Y. J. Sun, T. Nguyen, C. Lee and S. Soh, *Adv. Mater.*, 2018, **30**, 15.

22 D. J. Lacks and T. Shinbrot, *Nat. Rev. Chem.*, 2019, **3**, 465–476.

23 Y. Liu and B. X. Du, *IEEE Trans. Dielectr. Electr. Insul.*, 2010, **17**, 465–472.

24 Y. Zhang, C. H. Zhang, Y. Feng, T. D. Zhang, Q. G. Chen, Q. G. Chi, L. Z. Liu, G. F. Li, Y. Cui, X. Wang, Z. M. Dang and Q. Q. Lei, *Nano Energy*, 2019, **56**, 138–150.

25 Y. Li, X. Liu, X. Nie, W. Yang, Y. Wang, R. Yu and J. Shui, *Adv. Funct. Mater.*, 2019, **10**, 1807624.

26 X. Zhu, Z. Li, Y. Hu, H. Li, J. Yang and H. Lan, *Opt. Laser Technol.*, 2020, **123**, 105943.

27 X. Y. Zhu, Q. Xu, H. K. Li, M. Y. Liu, Z. H. Li, K. Yang, J. W. Zhao, L. Qian, Z. L. Peng, G. M. Zhang, J. J. Yang, F. Wang, D. C. Li and H. B. Lan, *Adv. Mater.*, 2019, **31**, 9.

28 B. Zhang, Q. Wang, Y. Zhang, W. Gao, Y. Hou and G. Zhang, *Nanoscale*, 2019, **11**, 18046–18051.

29 C. Wang, J. Guo, W. D. Li, X. R. Li, Z. H. Jiang, B. H. Guo and G. J. Zhang, *Mater. Lett.*, 2019, **249**, 17–20.

30 C. Wang, W. D. Li, J. Guo, X. Chen, Z.-H. Jiang, X. R. Li, B. H. Guo and G. J. Zhang, *Appl. Surf. Sci.*, 2019, **505**, 144432.

31 V. Jokinen, E. Kankuri, S. Hoshian, S. Franssila and R. H. A. Ras, *Adv. Mater.*, 2018, **30**, 10.

32 L. R. J. Scarratt, U. Steiner and C. Neto, *Adv. Colloid Interface Sci.*, 2017, **246**, 133–152.

33 A. Davis, Y. H. Yeong, A. Steele, I. S. Bayer and E. Loth, *ACS Appl. Mater. Interfaces*, 2014, **6**, 9272–9279.

34 Y. Wang, D. Y. Qiang, Z. Q. Xu, G. Chen and A. Vaughan, *J. Phys. D: Appl. Phys.*, 2018, **51**, 10.

35 W. W. Shen, H. B. Mu, G. J. Zhang, J. B. Deng and D. M. Tu, *J. Appl. Phys.*, 2013, **113**, 083706.

36 G. Y. Sun, B. P. Song, B. H. Guo, R. D. Zhou, S. Zhang, H. B. Mu and G. J. Zhang, *J. Phys. D: Appl. Phys.*, 2018, **51**, 295201.

37 J. R. Dennison and J. Brunson, *IEEE Trans. Plasma Sci.*, 2008, **36**, 2246–2252.

38 G. Blaise, *J. Electrost.*, 2001, **50**, 69–89.

39 R. D. Zhou, G. Y. Sun, B. P. Song, B. H. Guo, N. Yang, H. B. Mu and G. J. Zhang, *J. Phys. D: Appl. Phys.*, 2019, **52**, 375304.

40 B. H. Guo, G. Y. Sun, S. Zhang, J. Y. Xue, R. D. Zhou, B. P. Song, H. B. Mu and G. J. Zhang, *J. Phys. D: Appl. Phys.*, 2019, **52**, 215301.

41 Y. K. Huo, W. Y. Liu, C. F. Ke, C. Chang and C. H. Chen, *J. Appl. Phys.*, 2017, **122**, 115105.